Heliyon 9 (2023) e16741

Contents lists available at ScienceDirect

Heliyon

journal homepage: www.cell.com/heliyon

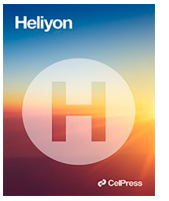

CFD analysis of heat transfer enhancement by wall mounted flexible flow modulators in a channel with pulsatile flow

Arpita Das, Fahim Tanfeez Mahmood, Rabeya Bosry Smriti, Sumon Saha, Mohammad Nasim Hasan *

Department of Mechanical Engineering, Bangladesh University of Engineering and Technology (BUET), Dhaka, 1000, Bangladesh

ARTICLE INFO

Keywords:
Flexible flow modulator
Pulsating flow
Arbitrary Lagrangian-Eulerian approach
Thermal enhancement
Power spectrum analysis

ABSTRACT

The aim of the present study is to explore heat transfer and pressure drop characteristics in a pulsating channel flow due to wall-mounted flexible flow modulators (FFM). Cold air in pulsating fashion is forced to enter through the channel having isothermally heated top and bottom walls with one/multiple FFMs mounted on them. The dynamic conditions of pulsating inflow are characterized by Reynolds number, non-dimensional pulsation frequency and amplitude. Applying the Galerkin finite element method in an Arbitrary Lagrangian-Eulerian (ALE) framework, the present unsteady problem has been solved. Flexibility ($10^{-4} \leq Ca \leq 10^{-7}$), orientation angle ($60^{\circ} \leq \theta \leq 120^{\circ}$), and location of FFM(s) have been considered in this study to find out the best-case scenario for heat transfer enhancement. The system characteristics have been analyzed by vorticity contours and isotherms. Heat transfer performance has been evaluated in terms of Nusselt number variations and pressure drop across the channel. Besides, power spectrum analysis of thermal field oscillation along with that of the FFM's motion induced by pulsating inflow has been performed. The present study reveals that single FFM having flexibility of $Ca = 10^{-5}$ and an orientation angle of $\theta = 90^{\circ}$ offers the best-case scenario for heat transfer enhancement.

1. Introduction

Recent developments in computational power have made it considerably simpler to predict fluid-flow phenomena based on the conservation laws of fluid motion. In addition, there has been an increase in numerous innovative techniques for thermal enhancement. Fluid-structure interaction (FSI), which accounts for the hydrodynamic effect of fluid and material deformation, is one such technique. Lately, the research community has been quite interested in heat exchangers due to its widespread usage in industrial systems such as solar thermal technology, chemical process, electrical device cooling, refrigeration systems, and so on. These systems, however, are not very thermally efficient on their own. Hence, various approaches for active or passive flow modulation have been introduced to facilitate heat transfer. FSI aids in this regard by modulating local vortices formed within the system and thereby promoting heat exchange. Meanwhile, pulsating flow provides another alternative means for thermal augmentation in case of flow through channels, pipes, or open/vented cavities. An overview of contemporary literature regarding application of flow modulators as well as flow pulsation for thermal performance enhancement of systems has been presented below.

* Corresponding author.
E-mail addresses: arpitaa.bd@gmail.com (A. Das), fahimtanfeez1610143@gmail.com (F.T. Mahmood), smritibosry@gmail.com (R.B. Smriti), sumonsaha@me.buet.ac.bd (S. Saha), nasim@me.buet.ac.bd (M.N. Hasan).

https://doi.org/10.1016/j.heliyon.2023.e16741
Received 5 November 2022; Received in revised form 19 April 2023; Accepted 25 May 2023
Available online 26 May 2023

1.1. Study on heat transfer enhancement incorporating rigid modulation

Thermal augmentation in a channel has received extensive study in numerous research works. Li et al. [1] explored heat transfer enhancement of a heated surface in an airflow channel with a vibrating piezo fan at Reynolds number, Re = 4000–30,000. They reported that when the Reynolds number was around $Re = 13{,}000$, thermal enhancement up to 147% was possible. Thermo-hydraulic assessment for Newtonian fluid flow in a corrugated channel under forced convection was carried out recently by Mehta and Pati [2]. They were able to achieve heat transfer enhancement as much as 428.93% from their corrugated channel when the dimensionless amplitude (α) and the wavelength (λ) of the wavy profile were $\alpha = 0.7$ and $\lambda = 0.5$ respectively, at $Re = 100$. As a way to increase fluid mixing and subsequently heat transfer by vortex generation, various studies incorporated rigid modulation [3,4]. Consequently, rigid fins [5] and baffles [6,7] were added in two- or three-dimensional channel systems to analyze the impacts of such rigid devices on heat transfer. Thermal augmentation of about 10 times along with an increased friction factor of 100 times were achieved from the rigid fin-channel system described in Ref. [5] at $Re = 500$. Similarly, the addition of baffles in a channel system of [7] accrued an increased pressure drop around 183.3% despite improving heat transfer by 350% at a blockage ratio of 0.5.

1.2. Study on heat transfer enhancement incorporating flexible modulation

Even though introduction of rigid modulators resulted in an appreciable amount of thermal improvement, a substantial pressure loss followed rendering the above-mentioned thermal systems ineffective. Therefore, to counteract this pressure drop effect, researchers turned to FSI investigations using flexible flow modulators. Inevitably, a multitude of flexible devices, including flexible baffles [8] and oscillating flexible fins [9–13] were added in stationary/lid-driven enclosures in recent years for comprehensive study. Thermal enhancement up to 101.69%, 200%, 280%, 8.5% and 3.29% respectively was possible from the systems of [8–12] when compared to the rigid modulator systems. Hence, these studies established that flexible flow modulators boosted heat transfer by stimulating vortex formation which could be attributed to their inertial effects. Afterwards, Park et al. [14] were also able to enhance heat transfer by 160% when installing a flexible flag in a Poiseuille flow-channel in expense of considerable mechanical energy loss (around 246%). Eventually, membranes or partitions were introduced in square [15–17], circular [18], and trapezoidal [19] enclosures and it was discovered that the increased FSI forces caused by the flexible membrane's deformation promoted forced convection. While exploring mixed convection in a cavity-channel arrangement, Sabbar et al. [20] discovered that the inclusion of flexible wall(s) facilitated heat transfer (around 17%). To assess the overall effectiveness of a partially compliant channel system, Ismail [21] opted to employ the widely used criterion known as thermal-hydraulic enhancement criterion (TEC). For such a channel system he reported a maximum value of TEC around 1.278 at Cauchy number $Ca = 10^{-7}$ and $Re = 250$.

1.3. Study on heat transfer enhancement incorporating flexible modulator's inclination

In addition to installing flexible modulators, their orientation plays a vital role on periodic vortex shedding as well as bulk fluid motion. Hence, Park [22] examined the influence of a flexible vortex generator's (VG) inclination angle and deduced that the increase in angle caused instabilities inside the system. This led to thermal enhancement of 117% accompanied with an increased energy loss of 179%. Following this, Song et al. [23] on their flat-plate film cooling found that cooling effectiveness became significant with the inclination of VG. They reported a 27.4% increase of cooling effectiveness when the inclination angle of VG was reduced from 40° to 20°. Ali et al. [24] while investigating the performance of a channel consisting of several inclined self-oscillating flexible vortex generators found 56% increase in thermal performance factor and 134% increase in the overall heat transfer.

1.4. Study on heat transfer enhancement utilizing pulsation flow

Adding pulsation to the flow is another active approach to increase heat transfer besides the insertion of rigid/flexible flow modulation devices [25]. Impact of pulsating flow in heat removal from two heated blocks installed in a channel was studied by Kim and Kang [26]. They found that increase in pulsating frequency, Strouhal number (St) heavily effected thermal enhancement and obtained up to 21% enhancement at $St = 0.8$ for the second block. Under a perturbation technique, Nield and Kuznetsov [27] explored forced convective heat transfer in a channel accompanied with a pulsatile flow and found that phase and magnitude of fluctuating Nusselt number changed with the dimensionless frequency. The effect of pulsating flow in channels of varying configurations [28–31] has also piqued the curiosity of several researchers recently. Later, from their investigation of forced convection in a wavy channel, Jafari et al. [32] reported that both the oscillation frequency and amplitude (A_{pulse}) played a crucial role on configuring flow and thermal fields. Consequently, they were able to obtain thermal enhancement up to 20% at $St = 0.25$ and $A_{pulse} = 0.25$. Selimefendigil and Oztop [33] studied the influence of pulsating flow over an adiabatic fin mounted on a backward-facing step and noticed heat transfer enhancement of 21% as well as increased dimensionless pressure drop $dP_m = 65$ at $St = 0.1$ and $A_{pulse} = 1.0$. Later Joshi et al. [34] incorporated twin flexible fins directly opposite to each other in a laminar pulsating channel flow and found maximum Nusselt number with flexible plate about 100% larger as compared to channel without fin. Eventually, magnetic field was introduced by Kolsi et al. [35] to demonstrate its influence on pulsating nanofluid flows in a corrugated bifurcating channel. Similarly, Hamzah and Sahin [36] analyze pulsating SWCNT-water nanofluid flow in a wavy channel. Recently, in an effort to experimentally study heat transfer augmentation in corrugated ducts Tokgoz and Sahin [37] employed Particle Image Velocimetry (PIV) technique to determine the influence of phase shifts (0◦ and 90◦) on the flow behavior. Afterwards, to experimentally explore convective heat transfer performance and hydrodynamics using PIV method Zontul and Sahin [38] introduced pulsation flow to their grooved channel. They inferred that

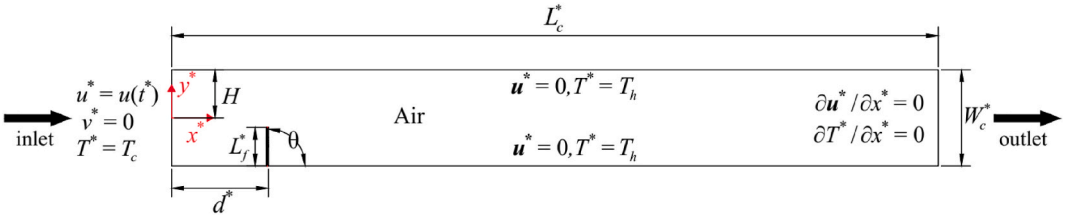

Fig. 1. Schematic diagram of the model (color online). (For interpretation of the references to color in this figure legend, the reader is referred to the Web version of this article.)

pulsating flow improves interaction between wake flow in groove and mainstream which resulted in increased heat transfer capability of the system due to better flow entrainment.

1.5. Scope of the present work

Although numerous studies discretely delineate the impact of flexible elements and flow pulsation on thermal enhancement, the cumulative effects of these phenomena have received little to no attention. Current investigation explores the impact of the orientation, flexibility, and various configurations of the flexible modulator under pulsating channel flow conditions. Moreover, influence of the pulsation frequency of the flow on the thermal as well as tip deflection frequency has been thoroughly analyzed with the help of power spectrum analysis. Also, the influences of flexibility, orientation, and configurations of the modulator on overall system performance have been given paramount importance.

The present computational fluid dynamics study incorporates the application of pulsating flow along with flow modulation by wall mounted FFM. To accurately capture the motion of FFM, the ALE framework [39,40] along with finite element analysis has been implemented.

2. Problem formulation and numerical modelling

2.1. Physical model

Fig. 1 depicts the setup of the current problem alongside the boundary conditions in a two-dimensional Cartesian system of co-ordinates represented by (x^*, y^*). In essence, the channel under study is a conduit of length $L^*_c = 16H$ [22,32] and width $W^*_c = 2H$. The computational rectangular domain spans from (0, $-H$) to (L^*_c, H), where H is the characteristic length and implies half of channel width. A FFM of length $L^*_f = 0.8H$ is installed to the bottom wall at various orientation angles (θ). The base of the modulator is secured at a distance $d^* = 2H$, and its free end is susceptible to deflection because of fluid's dynamic action by the incoming flow. It should be noted that air is considered as the working fluid for the present study.

2.2. Governing equations and assumptions

The fluid flow is considered to be laminar, two-dimensional, incompressible, Newtonian, and unsteady and the thermo-physical properties of the working fluid are presumed to be constant. The influences of buoyancy, magnetic field, thermal radiation, Joule heating, and viscous dissipation are ignored. By implementing the well-known ALE approach and applying the foregoing assumptions, the dimensional governing equations (1)–(4) are as follows:

For the fluid domain,

Continuity equation:

$$\nabla^* \cdot \boldsymbol{u}^* = 0, \tag{1}$$

Momentum equation:

$$\frac{\partial \boldsymbol{u}^*}{\partial t^*} + (\boldsymbol{u}^* - \boldsymbol{w}^*) \cdot \nabla^* \boldsymbol{u}^* = -\frac{1}{\rho_f} \nabla^* p^* + \nu_f \nabla^{*2} \boldsymbol{u}^*, \tag{2}$$

Energy equation:

$$\frac{\partial T^*}{\partial t^*} + (\boldsymbol{u}^* - \boldsymbol{w}^*) \cdot \nabla^* T^* = \alpha_f \nabla^{*2} T^*, \tag{3}$$

For the elastodynamic domain,

Displacement equation:

$$\rho_s \frac{d^2 \boldsymbol{d}_s^*}{dt^{*2}} - \nabla^* \boldsymbol{\sigma}^* = \boldsymbol{F}_v^*, \tag{4}$$

Table 1
Non-dimensional boundary conditions of the system.

Boundary conditions	Non-dimensional
Channel Walls	$\boldsymbol{u} = 0$ $T = 1$
Inlet	$u = 1 + A\sin(2\pi.St.t), v = 0$ $T = 0$
Outlet	$\partial \boldsymbol{u}/\partial x = 0$ $\partial T/\partial x = 0$ $p = 0$
Flow Modulator	$\partial \boldsymbol{d}_s/\partial t = \boldsymbol{u}$ $\frac{1}{Ca}\boldsymbol{\sigma}\cdot\boldsymbol{n} = -p + \frac{1}{Re}\nabla \boldsymbol{u}$

where $\boldsymbol{\sigma}^*$ denotes the stress tensor and $\boldsymbol{F}_v^*$ represents the body force vector acting on the mass of the modulator. Since the FFM is sufficiently thin and free from the effect of buoyancy force, the associated body force can be ignored [8,10]. Besides, $\boldsymbol{w}^*$ indicates the velocity of the moving coordinate, $\boldsymbol{u}^* = (u^*, v^*)$ denotes the fluid velocity vector, and $\boldsymbol{d}_s^*$ indicates the solid displacement vector. Also, p^*, T^*, α_f, ν_f and t^* represent fluid's pressure, temperature, thermal diffusivity, kinematic viscosity, and time respectively. The stress tensor $\boldsymbol{\sigma}^*$ exerted on the FFM due to the fluid flow can be calculated by equation (5) as follows:

$$\boldsymbol{\sigma}^* = J^{-1}FSF^T, \tag{5}$$

where $F = (I + \nabla^* \boldsymbol{d}_s^*), J = \det.(F)$, I represents the identity matrix and S is the Piola-Kirchhoff stress tensor that can be derived from the induced strain ε from equation (6) as follows:

$$S = C : (\varepsilon), \varepsilon = \frac{1}{2}\left(\nabla^* \boldsymbol{d}_s^* + \nabla^* \boldsymbol{d}_s^{*T} + \nabla^* \boldsymbol{d}_s^{*T}.\nabla^* \boldsymbol{d}_s^*\right), \tag{6}$$

where, C =C (E, ν) denotes the elasticity tensor where E and ν indicates the Elastic modulus and Poisson's ratio respectively. Also, the colon ':' in represents the double-dot tensor product.

By implementing dimensional analysis, the nondimensional governing equations (7)–(10) can be derived as follows [11]:

For the fluid domain,

$$\nabla \cdot \boldsymbol{u} = 0, \tag{7}$$

$$\frac{\partial \boldsymbol{u}}{\partial t} + (\boldsymbol{u} - \boldsymbol{w})\cdot\nabla \boldsymbol{u} = -\nabla p + \frac{1}{Re}\nabla^2 \boldsymbol{u}, \tag{8}$$

$$\frac{\partial T}{\partial t} + (\boldsymbol{u} - \boldsymbol{w})\cdot\nabla T = \frac{1}{RePr}\nabla^2 T, \tag{9}$$

For the elastodynamic domain,

$$\frac{Ca}{\rho_r}\frac{d^2 \boldsymbol{d}_s}{dt^2} - \nabla \boldsymbol{\sigma} = 0. \tag{10}$$

Dimensionless parameters and variables have been derived by normalizing them by following equation (11):

$$\begin{gathered}(x, y, L_f, L_c, d, W_c, \boldsymbol{d}_s) = \frac{\left(x^*, y^*, L_f^*, L_c^*, d^*, W_c^*, \boldsymbol{d}_s^*\right)}{H}, (\boldsymbol{u}, \boldsymbol{w}) = \frac{(\boldsymbol{u}^*, \boldsymbol{w}^*)}{u_o}, \\ p = \frac{p^*}{\rho_f u_o^2}, t = \frac{t^* u_o}{H}, T = \frac{T^* - T_c}{T_h - T_c}, \boldsymbol{\sigma} = \frac{\boldsymbol{\sigma}^*}{E}, \nabla = \nabla^* H,\end{gathered} \tag{11}$$

It is to be noted that all the symbols without superscript '*' represent dimensionless values of their corresponding dimensional counterparts. Here, $Pr = \nu_f/\alpha_f$ is the Prandtl number, $Re = u_o H/\nu_f$ denotes the Reynolds number (u_o being the mean inflow velocity), $Ca = \rho_f u_o^2/E$ represents the Cauchy number and $\rho_r = \rho_f/\rho_s$ yields the density ratio of fluid to solid structure. Here, ρ_f and ρ_s denotes density of the fluid and density of the FFM respectively.

2.3. System boundary and initial conditions

For proper depiction of the studied geometry, the boundary conditions of flow, thermal and displacement fields have been tabulated in Table 1 in non-dimensional form. The dimensionless flow frequency is modelled by Strouhal number $St = fH/u_o$, where f is the dimensional pulsatile frequency. Additionally, the term A represents the amplitude of inflow oscillation.

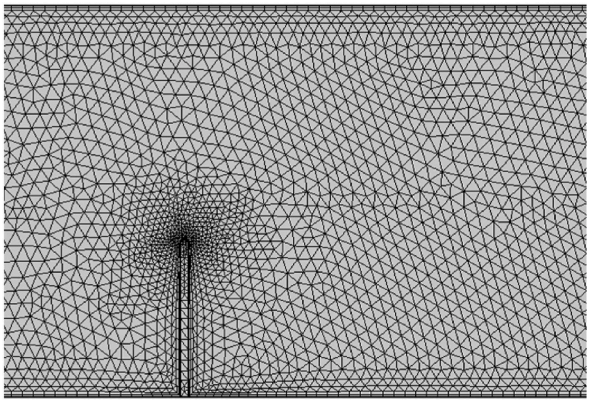

Fig. 2. Distribution of finite element mesh in the computational domain at the vicinity of FFM.

2.4. Vorticity

To study the hydrodynamics and flow structure of the system, vorticity field of the fluid flow has been analyzed [37,38]. The z-component of vorticity, ω_z has been evaluated using equation (12) given as:

$$\omega_z = \left(\frac{\partial v}{\partial x} - \frac{\partial u}{\partial y}\right). \tag{12}$$

2.5. Performance parameters

To investigate the heat transfer characteristics of the model, following Nusselt numbers have been evaluated utilizing following equations (13)–(15):

$$Nu_x(x,t) = \pm \left.\frac{\partial T}{\partial y}\right|_{y=1,-1}, \tag{13}$$

$$Nu(t) = \frac{1}{L_c}\int_0^{L_c} Nu_x(x,t)dx, \tag{14}$$

$$Nu_{avg} = \frac{1}{t_p}\int_0^{t_p} Nu(t)dt, \tag{15}$$

Here, $Nu_x(x,t)$ is the local Nusselt number, $Nu(t)$ is the spatially averaged Nusselt number and Nu_{avg} is the time averaged Nusselt number for a period of oscillation t_p.

The FFM experiences varied pressure drops as it deflects under fluctuating flow conditions. This pressure drop is evaluated by equations (16) and (17) as follows:

$$p_{in,avg} = \frac{1}{t_p}\int_0^{t_p} p_{in}(t)dt, \tag{16}$$

$$\Delta p = p_{in,avg} - p_{out,avg}, \tag{17}$$

Here, $P_{in}(t)$ is the inlet pressure, $P_{in,avg}$ and $P_{out,avg}$ are time averaged inlet and outlet pressures respectively, and ΔP is the pressure drop.

By considering this significant pressure drop, the overall thermal performance can be computed utilizing enhancement ratio (ER), pressure ratio (PR), and performance factor (PF) following [2,21,24] by implementing following equation (18):

$$ER = \frac{Nu_{avg}}{Nu_{o,avg}}, PR = \frac{\Delta p}{\Delta p_o}, PF = \frac{ER}{(PR)^{1/3}} \tag{18}$$

where, the subscript 'o' represents a system without any FFM.

Table 2
Comparison of average Nusselt number for various grid elements.

Elements	6345	9820	17,817	40,712	95,473
Nu_{avg}	7.593	8.039	8.307	**8.384**	8.403

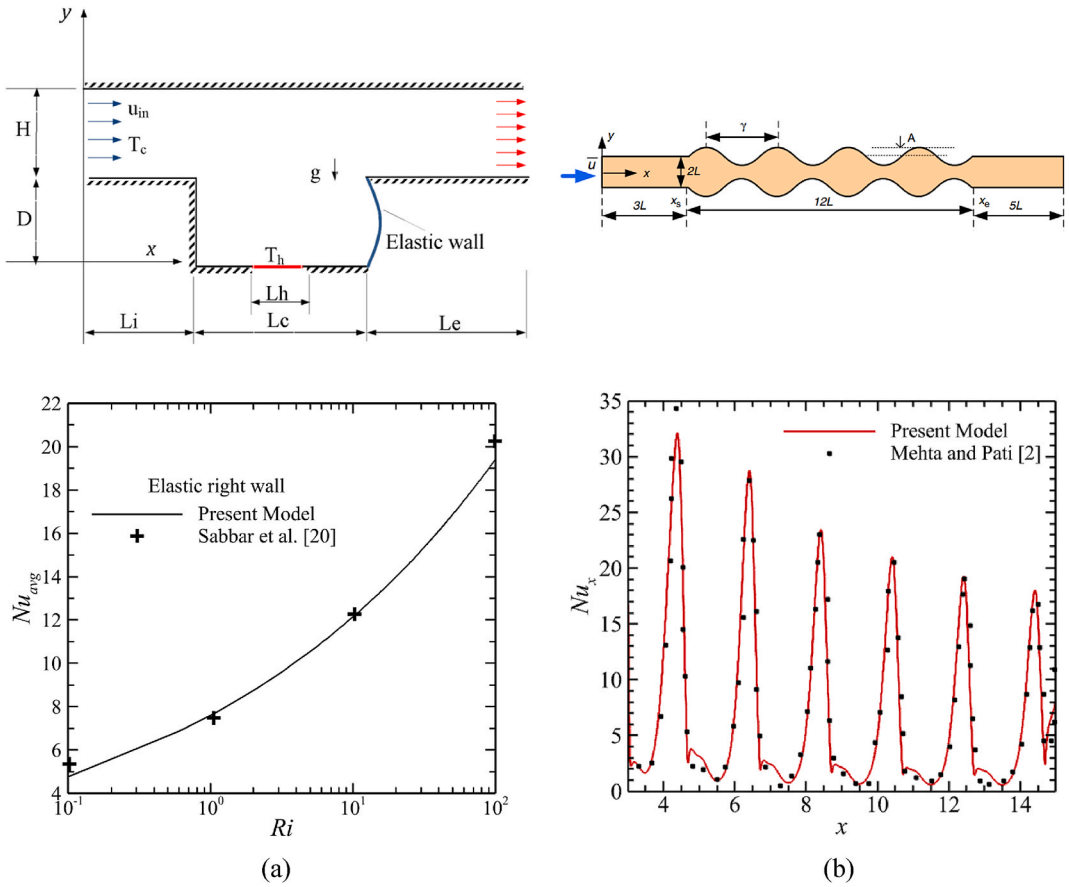

Fig. 3. Validation of the current model (a) in terms of Nu_{avg} against Sabbar et al. [20] where $Pr = 0.71$, $Re = 150$ and $Ca = 10^{-4}$ and (b) in terms of Nu_x against the wavy channel (amplitude, $\alpha = 0.5$ and wavelength, $\lambda = 1$) of Mehta and Pati [2] where $Pr = 20$, $Re = 100$ (color online). (For interpretation of the references to color in this figure legend, the reader is referred to the Web version of this article.)

3. Numerical methodology

The Galerkin finite element approach [39] has been utilized to model the nonlinear governing partial differential equations (1)–(4) and their respective dimensionless boundary conditions. A non-uniform grid incorporating boundary mesh refinement and composed of triangular and quadratic elements is used to discretize the computational domain, as portrayed partially in Fig. 2. The Arbitrary Lagrangian-Eulerian [40] method has been employed to adopt the moving mesh condition for capturing the oscillations and displacement of the FFM. To iteratively solve the residual finite element equations in each time-step (a constant time-step of 10^{-2}), the Newton-Raphson method is applied. The numerical solution is assumed to have converged when the sum of the residuals for all parameters is less than or equal to 10^{-7}. The numerical solution to the current problem is obtained using the finite element method-based software package "COMSOL Multiphysics 6.0".

3.1. Grid independence test

Several simulations have been performed for channel with single bottom wall mounted FFM with different mesh sizes while keeping parameters constant at $Pr = 0.71$, $Re = 200$, $Ca = 10^{-5}$, $\theta = 90°$, $A = 0.5$, and $St = 0.20$. From Table 2, it can be delineated that with the increase of domain elements, the value of average Nusselt number becomes almost constant. However, taking the accuracy and cost of computation into account, a non-uniform grid of 40,712 elements has been established as the optimum grid arrangement to acquire results throughout the study.

Table 3
Channels with different Flexible Flow Modulator (FFM) Configurations.

Case	Description
1	No FFM
2	Single FFM at bottom wall ($d = 2$, $y = -H$)
3	Double FFM ($d = 2$, $y = -H$), ($d = 4$, $y = H$)

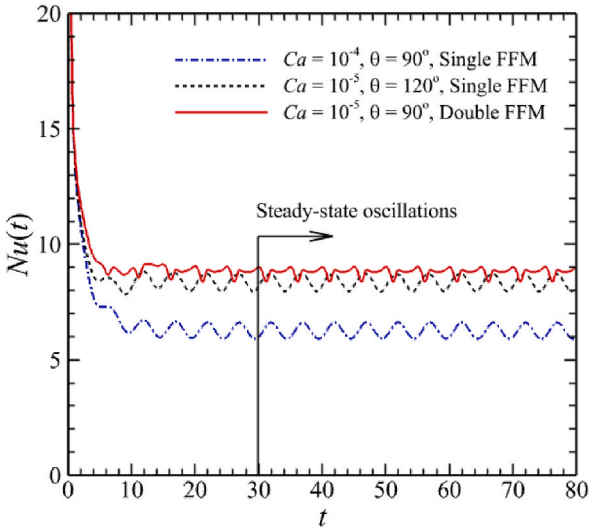

Fig. 4. Temporal variation of spatially averaged Nusselt number for several combinations of governing parameters (color online). (For interpretation of the references to color in this figure legend, the reader is referred to the Web version of this article.)

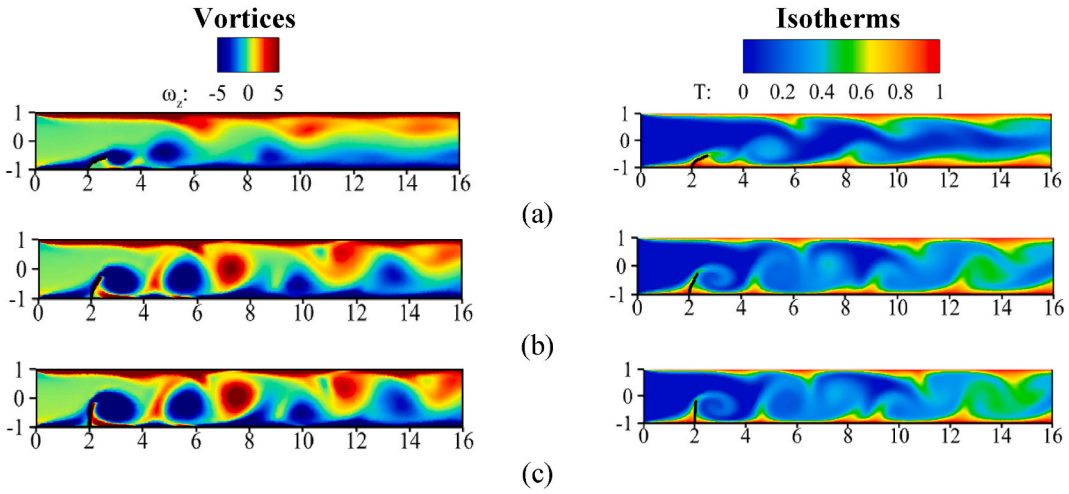

Fig. 5. Vortices and isotherms generated by single bottom wall mounted FFM ($\theta = 90°$) when modulator is at maximum deflected position for (a) $Ca = 10^{-4}$, (b) $Ca = 10^{-5}$ and (c) $Ca = 10^{-6}$ (color online). (For interpretation of the references to color in this figure legend, the reader is referred to the Web version of this article.)

3.2. Validation of model

To justify the FSI phenomenon, the current framework has been validated against the outcomes of Sabbar et al. [20] in terms of variation of average Nusselt number as depicted in Fig. 3(a) for a channel-cavity assembly. The cavity of the model consists of elastic side wall and a heating source at the bottom wall. It is fairly evident that the findings from the current model and those documented by Sabbar et al. [20] holds a good agreement. Moreover, another validation of corrugated channel model of Mehta and Pati [2] has justified the forced convective heat transfer in the current model. This literature studied forced convective heat transfer in a channel

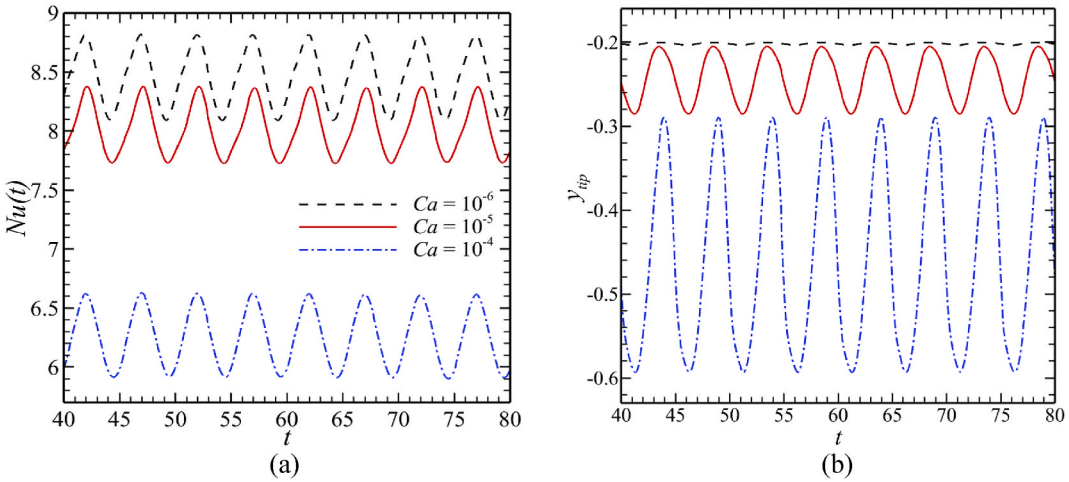

Fig. 6. Temporal variation of (a) $Nu(t)$ and (b) y_{tip} of single bottom wall mounted FFM at $\theta = 90^{\circ}$ for various Cauchy numbers (color online). (For interpretation of the references to color in this figure legend, the reader is referred to the Web version of this article.)

having isothermally heated wavy upper and lower wall. It can be observed in Fig. 3(b) that the evaluated average Nusselt number using the current model completely conforms with that of Mehta and Pati [2].

4. Results and discussions

This study has been carried out to investigate the influence of a FFM in a channel with pulsating air ($Pr = 0.71$) flowing through it. Hence, the modulator's flexibility, which is denoted by Ca, has been varied within the range of $10^{-4} \leq Ca \leq 10^{-7}$. Influence of the orientation angle of the FFM with respect to the bottom wall also has been investigated. Three orientation angles of $\theta = 60^{\circ}$, 90° and 120° have been considered in the current study. Moreover, this study has explored the impact of double FFM on flow field as compared to single FFM. Overall, three different configurations based on the presence of FFM have been explored as shown in Table 3. Throughout the study, the dynamic parameters of the flow field have been kept constant at Reynolds number $Re = 200$, non-dimensional pulsating frequency in terms of Strouhal number $St = 0.20$ and flow amplitude $A = 0.5$. All the outcomes have been evaluated at $t > 30$ since system reaches statistically steady-state condition after 30 for all the cases under consideration as presented in Fig. 4.

4.1. Impact of the flexibility of FFM

Flexibility of a flexible flow modulator is defined by Cauchy number which is inversely proportional to the elastic modulus. To investigate the influence of the flexibility of FFM, Ca has been varied from 10^{-7} to 10^{-4} for a single bottom wall mounted FFM oriented at $\theta = 90^{\circ}$.Vortices and isotherms for various value of Ca have been portrayed in Fig. 5. As can be seen, periodic vortices are generated in the downstream of the channel as a result of the interaction between the modulator and pulsating fluid flow. Since FFM is highly flexible at $Ca = 10^{-4}$, dynamic force of the flow field prevails the restoring force of the modulator. As a result, the modulator substantially leans toward the bottom wall. Furthermore, this flexible FFM weakly shears incoming fluid resulting in the development of weak vortices. These vortices sweep along the bottom wall without promoting enough mixing and fade out very quickly. Consequently, thicker thermal boundary layer is observed in the corresponding isotherm for $Ca = 10^{-4}$. Since the value of Ca decreases to 10^{-5} and owing to higher restoring force, FFM bends less toward the bottom wall and shears the incoming fluid strongly. Stronger vortices are generated at mid-section of the channel which promotes fluid mixing both at the upper and the lower walls. Hence, heat transfer increases and thinner thermal boundary layers are formed. Further decrease of Ca to 10^{-6} makes the FFM almost rigid. Therefore, very strong vortices are generated at the downstream and heat transfer enhances greatly as depicted by the corresponding isotherm.

To demonstrate the influence of the FFM on heat transfer and structural deformation, temporal variations of $Nu(t)$ along with y_{tip} (dimensionless vertical displacement of FFM's tip) have been portrayed in Fig. 6. Both parameters are oscillatory in nature due to pulsating flow condition. $Nu(t)$ obviously, becomes higher at a lower Ca which can be justified by the presence of stronger vortices. In addition, fluctuations of y_{tip} also diminishes at a lower value of Ca due to increased rigidity of FFM. Power spectrum analysis aided by fast Fourier transform (FFT) has been implemented for the corresponding thermal and tip deflection frequencies as shown in Fig. 7. From the observation of highest peak of FFT plots, it can be stated that both thermal and tip deflection frequencies are dominated by the pulsation frequency at $St = 0.20$. Since the FFM generates hardly any oscillations at $Ca = 10^{-6}$, the dominant peak is barely visible.

Since installation of an auxiliary device results in increased pressure drop, an overall performance analysis has been presented in Fig. 8 in terms of ER, PR, and PF. From Fig. 8(a) it can be observed that the value of ER rises with lower value of Ca until the increment becomes negligible beyond $Ca = 10^{-6}$. Therefore, beyond $Ca = 10^{-6}$, the modulator becomes rigid. Now, there is no further effect of elasticity of the modulator on heat transfer enhancement. PR plot in Fig. 8(b) also shows the similar trend, indicating pressure drop

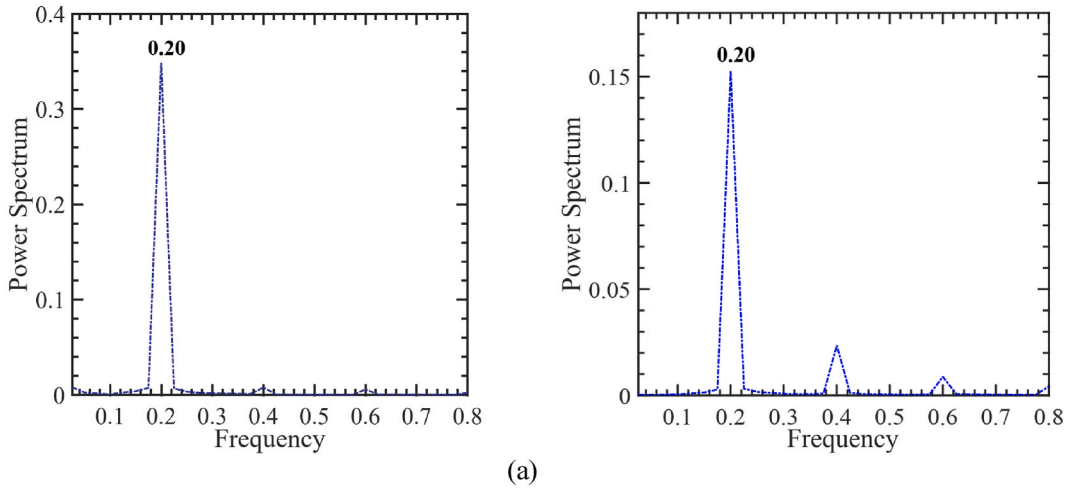

(a)

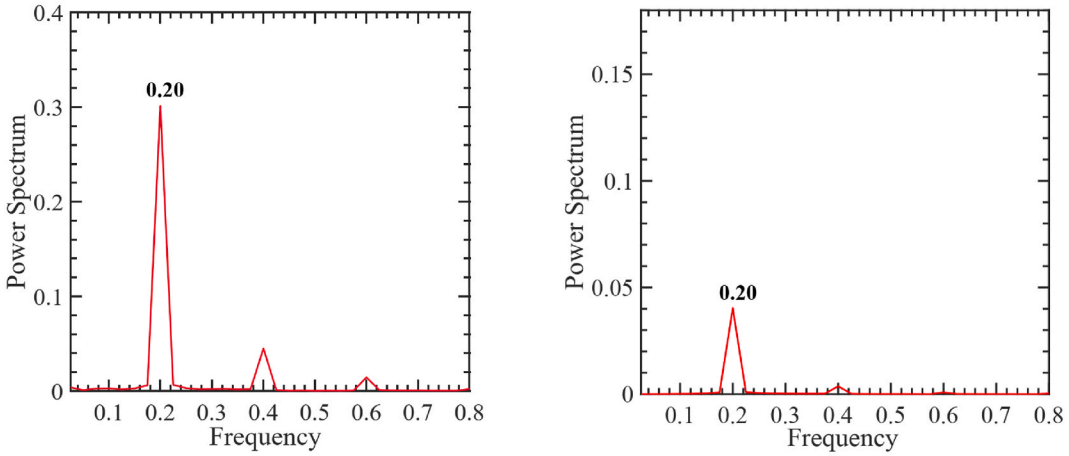

(b)

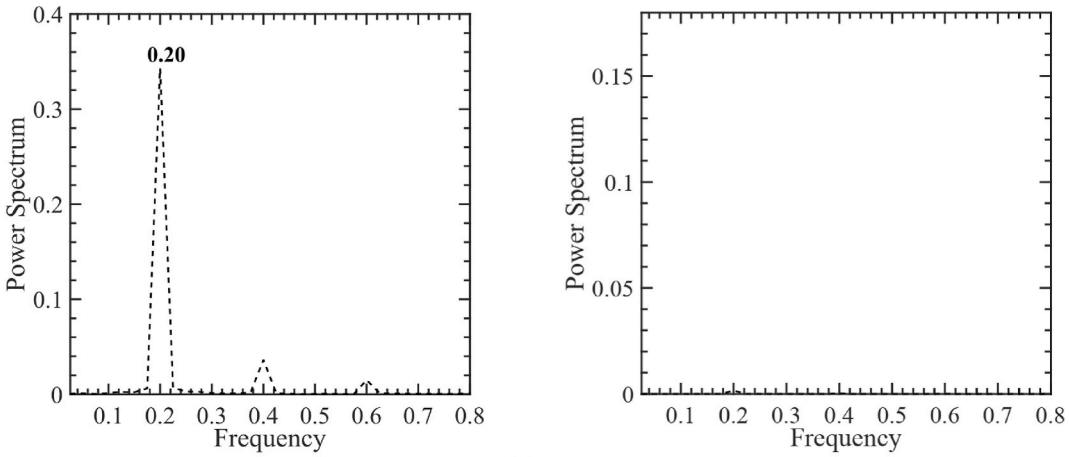

(c)

Fig. 7. Power spectrum analysis of the corresponding *Nu*(t) (left column) and y_{tip} (right column) from the same data in Fig. 6 for (a) $Ca = 10^{-4}$, (b) $Ca = 10^{-5}$ and (c) $Ca = 10^{-6}$ (color online). (For interpretation of the references to color in this figure legend, the reader is referred to the Web version of this article.)

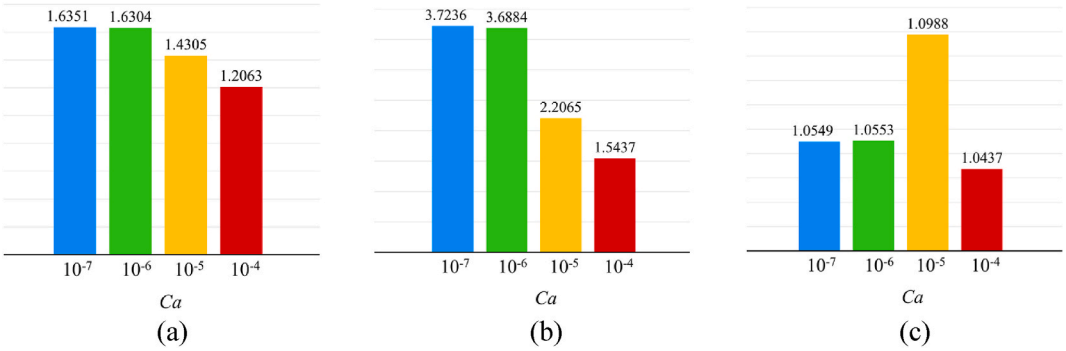

Fig. 8. Variations of (a) *ER*, (b) *PR*, and (c) *PF* with *Ca* for single bottom wall mounted FFM where $\theta = 90^{\circ}$ (color online). (For interpretation of the references to color in this figure legend, the reader is referred to the Web version of this article.)

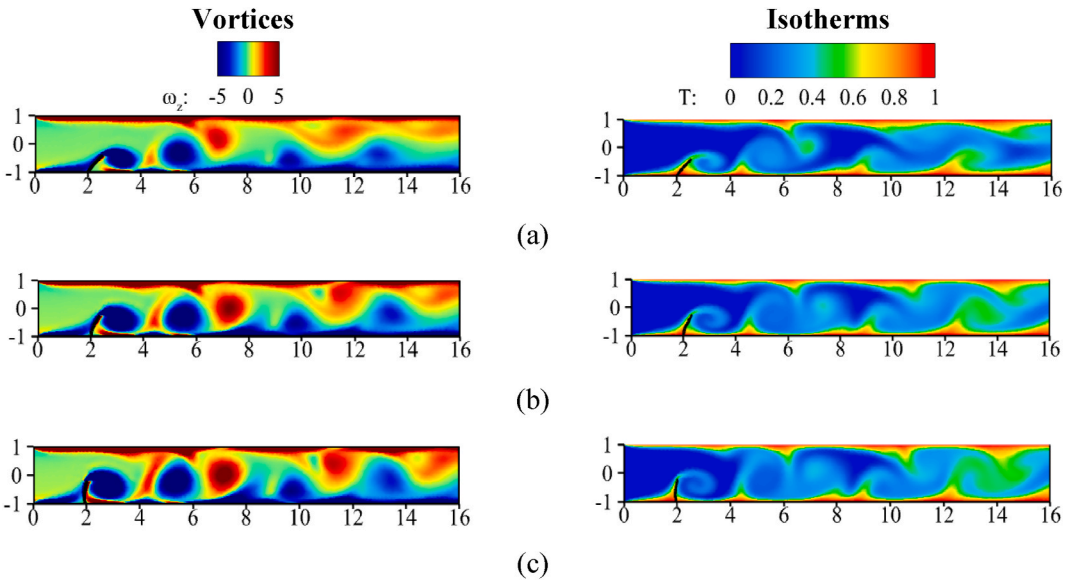

Fig. 9. Vortices and isotherms generated by single bottom wall mounted FFM when modulator is at maximum deflected position for (a) $\theta = 60^{\circ}$, (b) $\theta = 90^{\circ}$ and (c) $\theta = 120^{\circ}$ with $Ca = 10^{-5}$ (color online). (For interpretation of the references to color in this figure legend, the reader is referred to the Web version of this article.)

increases as the flexibility of the FFM reduces. Since a flexible FFM bends while oscillating, the region above it gets bigger. Hence, fluid flows through the channel with less obstruction which leads to lower pressure loss. On the other hand, for *Ca* beyond 10^{-6}, fluid flows through the narrower region above the rigid FFM which results in significant drop in pressure. Both *ER* and *PR* have essentially opposite impact on the system performance. Therefore, performance factor has been evaluated considering heat transfer enhancement and pressure drop as illustrated in Fig. 8(c). Although greater heat transfer enhancement is achieved when FFM becomes more rigid, pressure drop increases dramatically, which leads to the requirement of more pumping power. Thus, requirement of more mechanical energy offsets the enhancement on thermal performance. Consequently, lower *PF* is noticed when FFM gets more rigid. On the other hand, due to very poor heat transfer, highly flexible FFM also has lower *PF*. Hence, maximum performance factor is obtained at an optimum value of flexibility with about $Ca = 10^{-5}$.

4.2. *Influence of FFM's orientation*

Influence of FFM for orientation angles of $\theta = 60^{\circ}$, 90° and 120° have been explored in this section while keeping *Ca* fixed at 10^{-5}. From the visualization of vortices and isotherms in Fig. 9, it is apparent that when θ increases from 60° to 120°, the induced vortices get stronger. At $\theta = 60^{\circ}$, FFM is oriented along the flow direction and the obstruction to fluid flow caused by FFM is relatively less. Therefore, the generated vortices are comparatively weaker. When the value of θ increases to 90°, the region above the FFM become narrower. Incoming fluid is strongly sheared by the tip of the FFM resulting in stronger vortices. When $\theta = 120^{\circ}$, the FFM is oriented directly opposite to the flow direction of the incoming fluid. As a result, the incoming fluid is severely impeded leading to greater

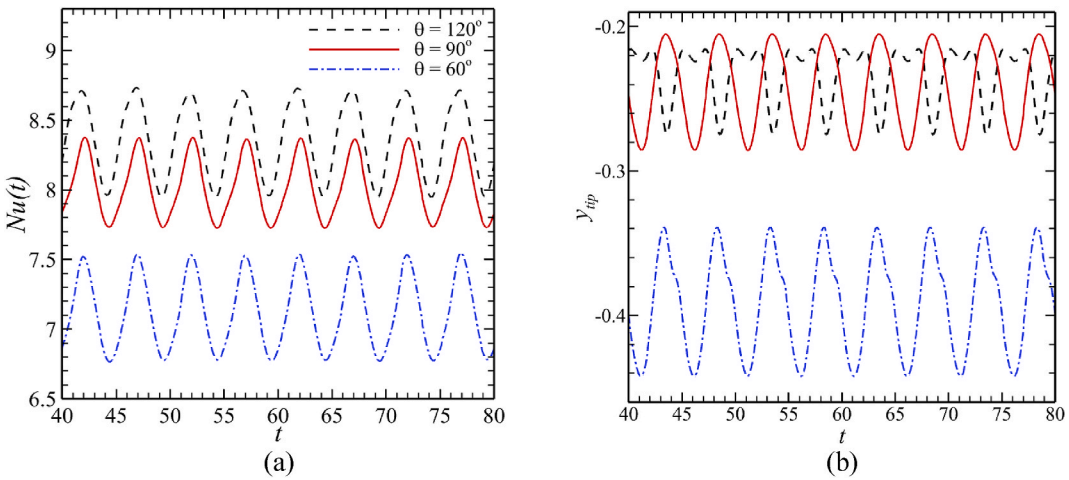

Fig. 10. Temporal variation of (a) $Nu(t)$ and (b) y_{tip} for single bottom wall mounted FFM at $Ca = 10^{-5}$ for various orientation angles (color online). (For interpretation of the references to color in this figure legend, the reader is referred to the Web version of this article.)

shearing and stronger vortices. Rapid fluid mixing is increased with the generation of stronger vortices which in turn causes thinning of thermal boundary layer. From the plot of isotherms in Fig. 9, it can be observed that thinnest thermal boundary is achieved at $\theta = 120^{\circ}$ and higher heat transfer is obtained at a larger value of θ.

To further investigate the trend of system performance that has been observed in Fig. 9, temporal variations of $Nu(t)$ and y_{tip} have been portrayed in Fig. 10 for different values of θ. Both $Nu(t)$ and y_{tip} show oscillatory nature as usual. When the value of θ increases, the curve of $Nu(t)$ shifts upward, due to enhancement of heat transfer rate enhances with FFM tilted more towards the entrance of the channel. In case of y_{tip}, amplitude of fluctuation for $\theta = 60^{\circ}$ is maximum since FFM is placed along the direction of the fluid flow. However, when $\theta = 120^{\circ}$, when FFM starts moving downward from the maximum position, a secondary fluctuation is introduced by the incoming fluid for a brief moment. Hence, the fluctuations for $\theta = 120^{\circ}$ is highly deviated from the sinusoidal pattern as compared to others. This phenomenon leads to the formation of stronger vortices at $\theta = 120^{\circ}$ and thus achieves highest heat transfer. To observe characteristics of thermal and flow induced frequencies of FFM, power spectrum analysis corresponding to the plots of $Nu(t)$ and y_{tip} have been performed and demonstrated in Fig. 11. For both $Nu(t)$ and y_{tip}, the dominant peak is prominent at a pulsating flow frequency of 0.20, whereas the non-dominant peaks are very insignificant. However, there is an exception in case of y_{tip} plot for $\theta = 120^{\circ}$, where a significant non-dominant peak at a frequency of 0.40 can be observed. This is because, for $\theta = 120^{\circ}$, there is a secondary fluctuation induced by the oscillation of tip deflection of the FFM.

Overall performance analysis of FFM at various orientation angles has been presented in Fig. 12. It is observed that both *ER* and *PR* show an ascending trend with increasing value of θ. Increasing trend of *ER* in Fig. 12(a) can be justified by the presence of stronger vortices at larger values of θ as portrayed in Fig. 9. Two different rising trends of *PR* are observed for θ between 60° and 120° in Fig. 12 (b). When θ goes from 60° to 90°, *PR* rises slowly at first, but then it rises dramatically as θ goes up to 120°. When FFM is positioned vertically ($\theta = 90^{\circ}$), the area above it gets smaller. However, it oscillates at a lower angle due to its flexibility which makes the area above it larger. Hence, the pressure drop is about the same as in case of $\theta = 60^{\circ}$. Now, when FFM is installed at $\theta = 120^{\circ}$ position, it substantially restricts the flow of the incoming fluid. Consequently, there is a substantial drop of pressure at $\theta = 120^{\circ}$. Fig. 12(c) demonstrates the overall performance factor after taking into consideration the improvement of heat transfer and the induced pressure drop. The value of *PF* rises till $\theta = 90^{\circ}$ and then sharply decreases when $\theta = 120^{\circ}$. The highest value of *PF* is obtained at about $\theta = 90^{\circ}$ since higher *ER* is obtained with comparatively lower *PR*. On the other hand, because of enormous drop in pressure, the value of *PF* is found to be minimum when FFM is placed at $\theta = 120^{\circ}$.

4.3. Comparisons of various FFM configurations

In this section, the channel with various FFM configurations as listed in Table 3 has been investigated. For all cases, modulator with $Ca = 10^{-5}$ has been installed vertically ($\theta = 90^{\circ}$). Vortices and isotherms for different cases have been depicted in Fig. 13. For case 1, thin sheet of vorticity can be observed since there is no FFM in the channel to facilitate vorticity generation. Hence, fluid mixing does not occur significantly which leads to formation of very thick thermal boundary layer. At Case 2, FFM placed at bottom wall, shed vortices near the bottom wall which in turn induce counter vortices near the top wall. For this case, very thin thermal boundary layer is observed at both top and bottom walls due to bulk fluid mixing. However, thermal boundary layer at bottom wall is comparatively thinner than that of top wall. Therefore, it can be said that the channel wall, on which FFM is installed, has a greater temperature gradient.

From the discussion so far, it can be inferred that the installation of a single FFM to a channel improves fluid mixing and heat transfer by a significant amount. For further investigation, Case 3 has been taken into consideration to assess the effects of simultaneously installing a top and bottom wall mounted FFM. In the case of a single FFM, the vortices it sheds induce counter vortices to form

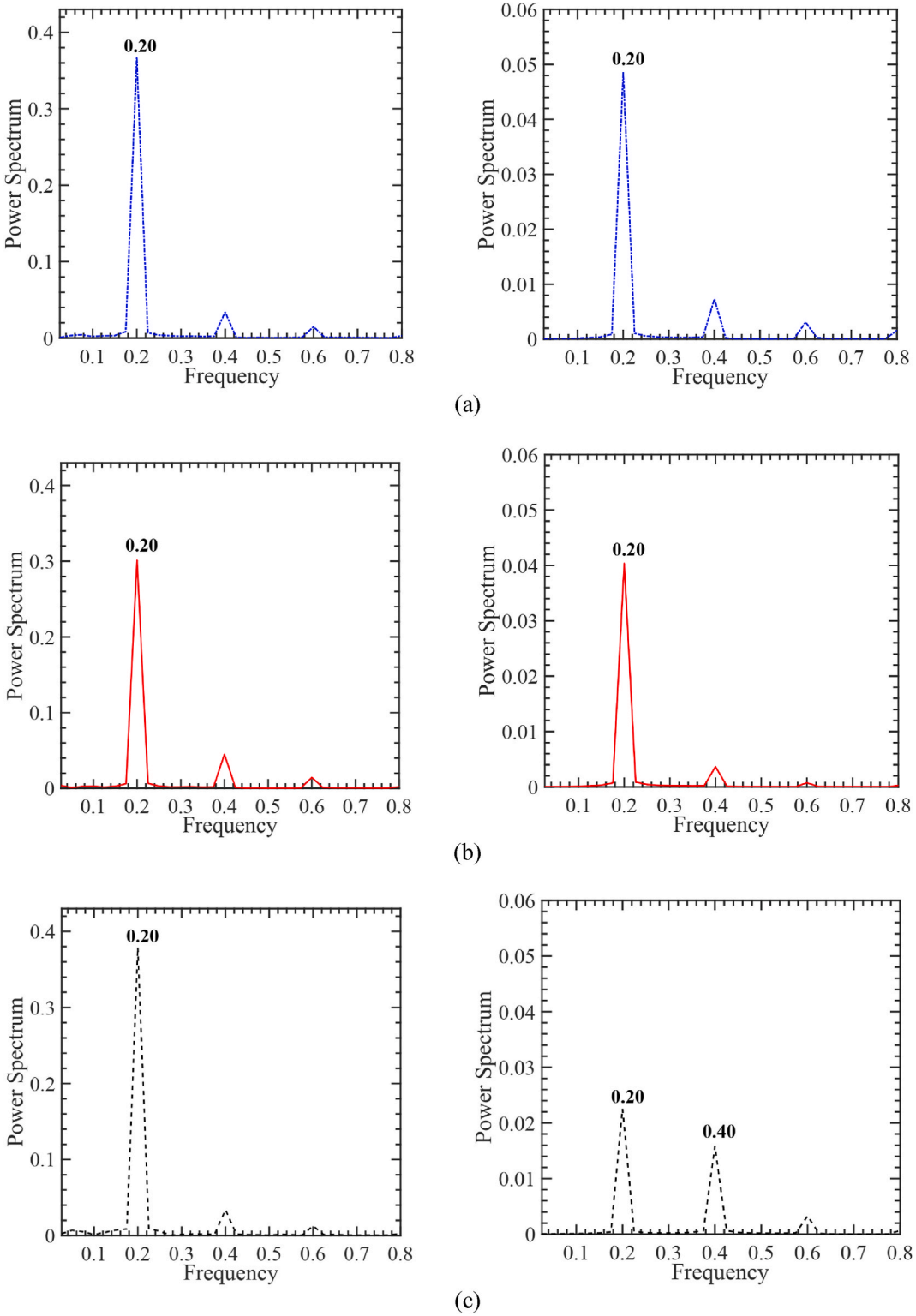

Fig. 11. Power spectrum analysis of the corresponding $Nu(t)$ (left column) and y_{tip} (right column) from the same data in Fig. 10 for (a) $\theta = 60^{\circ}$, (b) $\theta = 90^{\circ}$ and (c) $\theta = 120^{\circ}$ (color online). (For interpretation of the references to color in this figure legend, the reader is referred to the Web version of this article.)

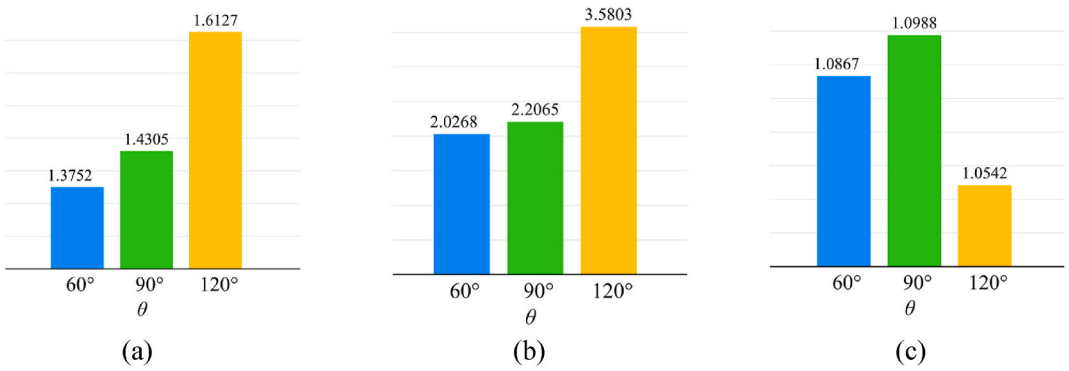

Fig. 12. Variations of (a) *ER*, (b) *PR*, and (c) *PF* with θ for single bottom wall mounted FFM ($Ca = 10^{-5}$) (color online). (For interpretation of the references to color in this figure legend, the reader is referred to the Web version of this article.)

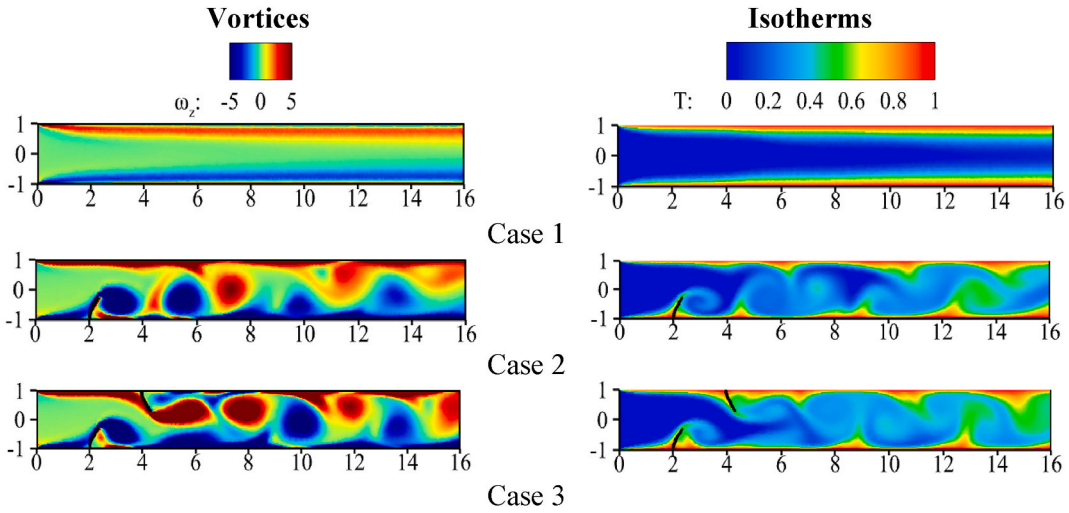

Fig. 13. Vortices and isotherms at various FFM configurations listed in Table 3 for $\theta = 90°$ and $Ca = 10^{-5}$ (color online). (For interpretation of the references to color in this figure legend, the reader is referred to the Web version of this article.)

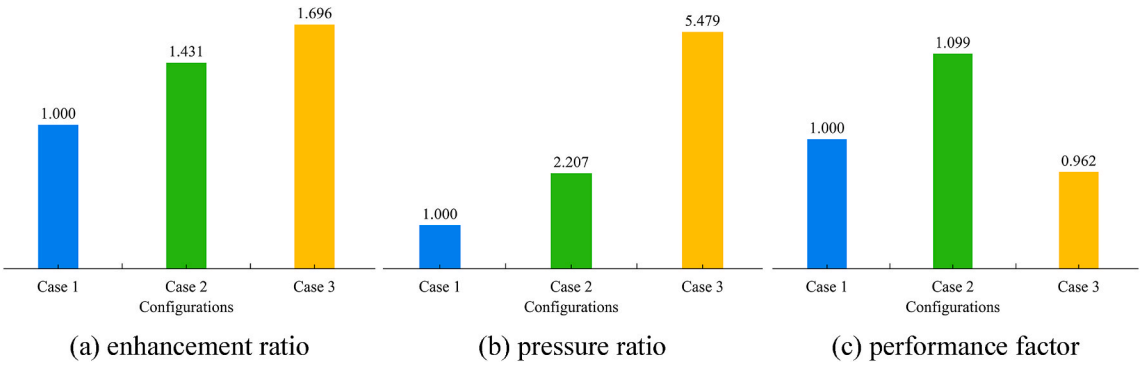

Fig. 14. Variations of (a) *ER*, (b) *PR*, and (c) *PF* with various configurations of FFM listed in Table 3 for $Ca = 10^{-5}$ and $\theta = 90°$ (color online). (For interpretation of the references to color in this figure legend, the reader is referred to the Web version of this article.)

at the opposing wall. However, in a channel with top and bottom wall-mounted modulators, the vortices at the walls are formed by direct solid-fluid interactions. As a result, vortices of equal strength are formed at both top and bottom wall. Consequently, fluid mixing enhances equally on both walls. Hence, thin thermal boundary layer of same thickness can be noticed in the corresponding isotherm plots. However, thick thermal boundary layer is observed near the FFM that is placed at further distance in Case 3. This is due to the

previously produced vortex of the prior FFM obstructing the vortex shed by the later FFM, henceforth, impeding the fluid mixing.

Overall performance analysis of these three configurations has been presented in Fig. 14 in terms of *ER*, *PR* and *PF*. Fig. 14(a) shows that the channel with modulators achieve always higher heat transfer than the channel without any. Among all cases, channels with double FFM offer the maximum heat transfer enhancement. However, a pressure drop of significant amount offsets this outcome that can be seen in Fig. 14(b). One can notice that the pressure drop in double FFM configuration is almost twice as compared to the single FFM case. Since fluid flow is highly impeded by the top and the bottom FFMs, significant amount of pumping work would require to deliver the fluid through the channel. From the *PF* plot as shown in Fig. 14(c), it can be asserted that the best possible thermal performance can be attained with a bottom wall mounted FFM which is around 10%. Due to huge pressure drop in Case 3, its contributions to heat transfer enhancement become expensive. In fact, *PF* drops below 1 for Case 3, which indicates very poor efficiency of the system. Therefore, it could be concluded that single bottom wall mounted FFM having flexibility of $Ca = 10^{-5}$ and orientation angle of 90° offers the best-case scenario for heat transfer enhancement.

5. Conclusions

The current study explores the impact of flexible flow modulator on heat transfer enhancement in a straight channel with isothermally heated upper and lower walls which are subjected to pulsating air flow. The fluid flow is considered to be two-dimensional laminar, incompressible, Newtonian, and the thermo-physical properties of the working fluid are presumed to be constant. Non-dimensional flow amplitude and pulsation frequency have been kept constant at $A = 0.5$ and $St = 0.20$, respectively. Galerkin finite element method in an Arbitrary Lagrangian-Eulerian framework has been applied to numerically solve the present unsteady problem. This study has thoroughly investigated the impacts of flexibility ($10^{-4} \leq Ca \leq 10^{-7}$), orientation angle ($60° \leq \theta \leq 120°$) and different configurations of FFM. The flow field has been visualized with the help of vorticity contour and isotherm plots. Moreover, power spectrum analysis has been performed for interpreting induced thermal and tip deflection frequencies. Overall performance analysis has also been done by accounting both the heat transfer enhancement and pressure drop across the channel.

Following remarks can be drawn from the present study:

- FFM with an optimum flexibility of $Ca = 10^{-5}$ is most suitable for thermal augmentation in a channel. Highly rigid or flexible modulator deteriorates the performance of the system.
- Frequencies of thermal field and induced tip deflection of FFM have been found conforming to the imposed pulsating inflow frequency ($St = 0.20$).
- Among various orientation angles of the FFM, a vertically oriented FFM ($\theta = 90°$) offers better heat transfer enhancement with a reasonable pressure drop.
- Although channels with double FFM achieves highest heat transfer, the corresponding pressure drop is huge. As a result, the overall performance of the system drastically deteriorates.
- The channel with a single bottom-wall mounted FFM achieves the best overall performance among the various configurations, which is about 10% higher compared to a channel without modulator.

Author contribution statement

Arpita Das: Fahim Tanfeez Mahmood: Rabeya Bosry Smriti: Performed the experiments; Analyzed and interpreted the data; Wrote the paper.

Sumon Saha: Analyzed and interpreted the data; Contributed reagents, materials, analysis tools or data; Wrote the paper.

Mohammad Nasim Hasan: Conceived and designed the experiments; Analyzed and interpreted the data; Contributed reagents, materials, analysis tools or data; Wrote the paper.

Data availability statement

Data will be made available on request.

Declaration of competing interest

The authors declare that they have no known competing financial interests or personal relationships that could have appeared to influence the work reported in this paper

Acknowledgement

The authors gratefully acknowledge Basic Research Grant provided by Bangladesh University of Engineering and Technology [Office Order: 5336(100)-Sl. 23; Dated June 30, 2021]. The authors appreciate CFDHT Research Group, Department of Mechanical Engineering Bangladesh University of Engineering and Technology (BUET) for thoughtful discussion and support in conducting this research.

Nomenclature

Roman Symbols

A	Amplitude
Ca	Cauchy number
d	Distance of modulator from channel inlet
$\boldsymbol{d_s}$	Displacements vector
ER	Enhancement ratio
$\boldsymbol{F_v}$	Body force vector
k	Thermal conductivity
L_c	Channel length
L_f	Length of flow modulator
$\boldsymbol{n}$	Normal vector
$Nu(t)$	Spatially averaged Nusselt number
Nu_{avg}	Time averaged Nusselt number
Nu_x	Local Nusselt number
p	Pressure
$P(t)$	Spatially averaged inlet pressure
PF	Performance factor
$P_{in,avg}$	Time averaged inlet pressure
Pr	Prandtl number
PR	Pressure ratio
Re	Reynolds number
St	Strouhal number
t	Time
T	Dimensionless temperature
u	Horizontal velocity component
$\boldsymbol{u}$	Velocity vector
v	Vertical velocity component
$\boldsymbol{w}$	Moving co-ordinate velocity vector
W_c	Channel width
x,y	Cartesian coordinates
y_{tip}	Dimensionless horizontal/vertical displacement of flow modulator tip
ΔP	Pressure drop

Greek Symbols

α_f	Thermal diffusivity of fluid
υ	Poisson's ratio
ν_f	Momentum diffusivity of fluid
ω_z	z-component of vorticity field
ρ_f	Fluid density
ρ_r	Density ratio
ρ_s	Solid density
σ	Stress tensor
θ	Orientation angle of FFM

Superscript

*	Dimensional parameters

Subscript

Bottom	Along bottom wall
c	Cold
f	Fluid
h	Hot
o	System without flow modulator
Top	Along top wall

Abbreviations

ALE	Arbitrary Langrangian-Eulerian
FFT	Fast Fourier Transform
FSI	Fluid-Structure Interaction

FFM Flexible Flow Modulator
VG Vortex Generator

References

[1] X.-J. Li, J. Zhang, X. Tan, Y. Wang, Enhancing forced-convection heat transfer of a channel surface with piezo-fans, Int. J. Mech. Sci. 227 (2022) 107437, https://doi.org/10.1016/j.ijmecsci.2022.107437.

[2] S.K. Mehta, S. Pati, Numerical study of thermo-hydraulic characteristics for forced convective flow through wavy channel at different Prandtl numbers, J. Therm. Anal. Calorim. 141 (6) (2020) 2429–2451, https://doi.org/10.1007/s10973-020-09412-5.

[3] G. Biswas, H. Laschefski, N.K. Mitra, M. Fiebig, Numerical investigation of mixed convection heat transfer in a horizontal channel with a built-in square cylinder, Numer. Heat Transf. A Appl. 18 (2) (1990) 173–188, https://doi.org/10.1080/10407789008944789.

[4] P.-Y. Xiong, A. Hamid, K. Iqbal, M. Irfan, M. Khan, Numerical simulation of mixed convection flow and heat transfer in the lid-driven triangular cavity with different obstacle configurations, Int. Commun. Heat Mass Tran. 123 (2021) 105202, https://doi.org/10.1016/j.icheatmasstransfer.2021.105202.

[5] C. Chin-Hsiang, H. Wen-Hsiung, Numerical prediction for laminar forced convection in parallel-plate channels with transverse fin arrays, Int. J. Heat Mass Tran. 34 (11) (1991) 2739–2749, https://doi.org/10.1016/0017-9310(91)90232-4.

[6] Z. Guo, N.K. Anand, Three-dimensional heat transfer in a channel with a baffle in the entrance region, Numer. Heat Transf. A Appl. 31 (1) (1997) 21–35, https://doi.org/10.1080/10407789708914023.

[7] S.S. Mousavi, K. Hooman, Heat and fluid flow in entrance region of a channel with staggered baffles, Energy Convers. Manag. 47 (15–16) (2006) 2011–2019, https://doi.org/10.1016/j.enconman.2005.12.018.

[8] A. Raisi, I. Arvin, A numerical study of the effect of fluid-structure interaction on transient natural convection in an air-filled square cavity, Int. J. Therm. Sci. 128 (2018) 1–14, https://doi.org/10.1016/j.ijthermalsci.2018.02.012.

[9] M. Ghalambaz, E. Jamesahar, M.A. Ismael, A.J. Chamkha, Fluid-structure interaction study of natural convection heat transfer over a flexible oscillating fin in a square cavity, Int. J. Therm. Sci. 111 (2017) 256–273, https://doi.org/10.1016/j.ijthermalsci.2016.09.001.

[10] Md.A. Hakim, A.I. Ahad, A.U. Karim, S. Saha, M.N. Hasan, Fluid structure interaction and heat transfer enhancement with dynamic flexible flow modulator, Int. Commun. Heat Mass Tran. 134 (2022), 105983, https://doi.org/10.1016/j.icheatmasstransfer.2022.105983.

[11] M.A. Ismael, H.F. Jasim, Role of the fluid-structure interaction in mixed convection in a vented cavity, Int. J. Mech. Sci. 135 (2018) 190–202, https://doi.org/10.1016/j.ijmecsci.2017.11.001.

[12] E. Jamesahar, M. Sabour, M. Shahabadi, S.A.M. Mehryan, M. Ghalambaz, Mixed convection heat transfer by nanofluids in a cavity with two oscillating flexible fins: a fluid–structure interaction approach, Appl. Math. Model. 82 (2020) 72–90, https://doi.org/10.1016/j.apm.2019.12.018.

[13] X. Shi, J.M. Khodadadi, Periodic state of fluid flow and heat transfer in a lid-driven cavity due to an oscillating thin fin, Int. J. Heat Mass Tran. 48 (25–26) (2005) 5323–5337, https://doi.org/10.1016/j.ijheatmasstransfer.2005.07.026.

[14] S.G. Park, B. Kim, C.B. Chang, J. Ryu, H.J. Sung, Enhancement of heat transfer by a self-oscillating inverted flag in a Poiseuille channel flow, Int. J. Heat Mass Tran. 96 (2016) 362–370, https://doi.org/10.1016/j.ijheatmasstransfer.2016.01.043.

[15] E. Jamesahar, M. Ghalambaz, A.J. Chamkha, Fluid–solid interaction in natural convection heat transfer in a square cavity with a perfectly thermal-conductive flexible diagonal partition, Int. J. Heat Mass Tran. 100 (2016) 303–319, https://doi.org/10.1016/j.ijheatmasstransfer.2016.04.046.

[16] S.A.M. Mehryan, M. Ghalambaz, M.A. Ismael, A.J. Chamkha, Analysis of fluid-solid interaction in MHD natural convection in a square cavity equally partitioned by a vertical flexible membrane, J. Magn. Magn Mater. 424 (2017) 161–173, https://doi.org/10.1016/j.jmmm.2016.09.123.

[17] M. Ghalambaz, S.A.M. Mehryan, M.A. Ismael, A. Chamkha, D. Wen, Fluid–structure interaction of free convection in a square cavity divided by a flexible membrane and subjected to sinusoidal temperature heating, Int. J. Numer. Methods Heat Fluid Flow 30 (6) (2020) 2883–2911, https://doi.org/10.1108/HFF-12-2018-0826.

[18] A.B. Shahrestani, B. Alshuraiaan, M. Izadi, Combined natural convection-FSI inside a circular enclosure divided by a movable barrier, Int. Commun. Heat Mass Tran. 126 (2021) 105426, https://doi.org/10.1016/j.icheatmasstransfer.2021.105426.

[19] S.A.M. Mehryan, M. Ghalambaz, R. Kalantar Feeoj, A. Hajjar, M. Izadi, Free convection in a trapezoidal enclosure divided by a flexible partition, Int. J. Heat Mass Tran. 149 (2020) 119186, https://doi.org/10.1016/j.ijheatmasstransfer.2019.119186.

[20] W.A. Sabbar, M.A. Ismael, M. Almudhaffar, Fluid-structure interaction of mixed convection in a cavity-channel assembly of flexible wall, Int. J. Mech. Sci. 149 (2018) 73–83, https://doi.org/10.1016/j.ijmecsci.2018.09.041.

[21] M.A. Ismael, Forced convection in partially compliant channel with two alternated baffles, Int. J. Heat Mass Tran. 142 (2019) 118455, https://doi.org/10.1016/j.ijheatmasstransfer.2019.118455.

[22] S.G. Park, Heat transfer enhancement by a wall-mounted flexible vortex generator with an inclination angle, Int. J. Heat Mass Tran. 148 (2020) 119053, https://doi.org/10.1016/j.ijheatmasstransfer.2019.119053.

[23] L. Song, C. Zhang, Y. Song, J. Li, Z. Feng, Experimental investigations on the effects of inclination angle and blowing ratio on the flat-plate film cooling enhancement using the vortex generator downstream, Appl. Therm. Eng. 119 (2017) 573–584, https://doi.org/10.1016/j.applthermaleng.2017.03.089.

[24] S. Ali, C. Habchi, S. Menanteau, T. Lemenand, J.L. Harion, Heat transfer and mixing enhancement by free elastic flaps oscillation, Int. J. Heat Mass Tran. 85 (2015) 250–264, https://doi.org/10.1016/J.IJHEATMASSTRANSFER.2015.01.122.

[25] Q. Ye, Y. Zhang, J. Wei, A comprehensive review of pulsating flow on heat transfer enhancement, Appl. Therm. Eng. 196 (2021) 117275, https://doi.org/10.1016/J.APPLTHERMALENG.2021.117275.

[26] S.Y. Kim, B.H. Kang, J.M. Hyun, Forced convection heat transfer from two heated blocks in pulsating channel flow, Int. J. Heat Mass Tran. 41 (3) (1998) 625–634, https://doi.org/10.1016/S0017-9310(97)00138-5.

[27] D.A. Nield, A.V. Kuznetsov, Forced convection with laminar pulsating flow in a channel or tube, Int. J. Therm. Sci. 46 (6) (2007) 551–560, https://doi.org/10.1016/j.ijthermalsci.2006.07.011.

[28] N. Kurtulmuş, B. Sahin, Experimental investigation of pulsating flow structures and heat transfer characteristics in sinusoidal channels, Int. J. Mech. Sci. 167 (2020) 105268, https://doi.org/10.1016/j.ijmecsci.2019.105268.

[29] C.S. Wang, C.C. Chen, W.C. Chang, T.M. Liou, Experimental studies of turbulent pulsating flow and heat transfer in a serpentine channel with winglike turbulators, Int. Commun. Heat Mass Tran. 131 (2022) 105837, https://doi.org/10.1016/j.icheatmasstransfer.2021.105837.

[30] S. Akcay, Numerical analysis of heat transfer improvement for pulsating flow in a periodic corrugated channel with discrete V-type winglets, Int. Commun. Heat Mass Tran. 134 (2022), 105991, https://doi.org/10.1016/j.icheatmasstransfer.2022.105991.

[31] H.H. Afrouzi, M. Ahmadian, A. Moshfegh, D. Toghraie, A. Javadzadegan, Statistical analysis of pulsating non-Newtonian flow in a corrugated channel using Lattice-Boltzmann method, Phys. Stat. Mech. Appl. 535 (2019) 122486, https://doi.org/10.1016/J.PHYSA.2019.122486.

[32] M. Jafari, M. Farhadi, K. Sedighi, Pulsating flow effects on convection heat transfer in a corrugated channel: a LBM approach, Int. Commun. Heat Mass Tran. 45 (2013) 146–154, https://doi.org/10.1016/j.icheatmasstransfer.2013.04.006.

[33] F. Selimefendigil, H.F. Öztop, Numerical analysis of laminar pulsating flow at a backward facing step with an upper wall mounted adiabatic thin fin, Comput. Fluids 88 (2013) 93–107, https://doi.org/10.1016/j.compfluid.2013.08.013.

[34] R.U. Joshi, A.K. Soti, R. Bhardwaj, Convective heat transfer augmentation by flexible fins in laminar channel pulsating flow, in: Proceedings of CHT-15. 6th International Symposium on Advances in Computational Heat Transfer, 2015, pp. 1623–1634, https://doi.org/10.1615/ICHMT.2015.INTSYMPADVCOMPUTHEATTRANSF.1570.

[35] L. Kolsi, F. Selimefendigil, K. Ghachem, T. Alqahtani, S. Algarni, Pulsating nanofluid flow in a wavy bifurcating channel under partially active uniform magnetic field effects, Int. Commun. Heat Mass Tran. 133 (2022) 105938, https://doi.org/10.1016/j.icheatmasstransfer.2022.105938.
[36] H. Hamzah, B. Sahin, Analysis of SWCNT-water nanofluid flow in wavy channel under turbulent pulsating conditions: investigation of homogeneous and discrete phase models, Int. J. Therm. Sci. 184 (2023) 108011, https://doi.org/10.1016/J.IJTHERMALSCI.2022.108011.
[37] N. Tokgoz, B. Sahin, Experimental studies of flow characteristics in corrugated ducts, Int. Commun. Heat Mass Tran. 104 (2019) 41–50, https://doi.org/10.1016/j.icheatmasstransfer.2019.03.003.
[38] H. Zontul, B. Şahin, Experimental investigation of convective heat transfer performance and hydrodynamics of pulsating flow through the rectangular grooved channel, Exp. Therm. Fluid Sci. 141 (2023) 110796, https://doi.org/10.1016/j.expthermflusci.2022.110796.
[39] G.J. Fix, Finite Element Methods for Flow Problems, 1982, pp. 28–29, https://doi.org/10.1002/0470013826.
[40] C.W. Hirt, A.A. Amsden, J.L. Cook, An arbitrary Lagrangian-Eulerian computing method for all flow speeds, J. Comput. Phys. 14 (3) (1974) 227–253, https://doi.org/10.1016/0021-9991(74)90051-5.